Journal of ELECTRONIC MATERIALS, Vol. 49, No. 9, 2020
https://doi.org/10.1007/s11664-020-08259-8

TOPICAL COLLECTION: 18TH CONFERENCE ON DEFECTS (DRIP XVIII)

Cathodoluminescence Study of Dislocations in Step-Graded InGaP Buffer Layers of Metamorphic Single-Junction InGaAs Solar Cells

A. OGURA,[1,4] W. YI,[2] J. CHEN,[2] H. SUZUKI,[3] and M. IMAIZUMI[1]

1.—Japan Aerospace Exploration Agency, Tsukuba, Ibaraki 305-8505, Japan. 2.—National Institute for Materials Science, Tsukuba, Ibaraki 305-0044, Japan. 3.—Faculty of Engineering, University of Miyazaki, Miyazaki 889-2192, Japan. 4.—e-mail: ogura.akio@jaxa.jp

Epitaxial growth of lattice-mismatched materials is useful for solar cells, but lattice dislocations must be controlled for best device performance. It has been shown that metamorphic growth enables fabrication of InGaAs *p*–*n* junctions with good performances on GaAs substrates due to the insertion of buffer layers. Here, we investigate misfit and threading dislocations inside the step-graded InGaP buffer layers of a single-junction InGaAs solar cell by cathodoluminescence microscopy. Prior to measurement, the device edges were polished at various angles (less than 10° with respect to the substrate surface). By using this technique, cross sections of very thin layers can be directly imaged with a resolution that allows us to observe misfit and threading dislocations. In the present device, the densities of the two types of dark lines depend on the position in the buffer structure. In particular, near the InGaAs base layer, the density of the dark lines extending in the [110] direction is higher than that of the dark lines extending in the [1-10] direction. We believe that this difference in the dark line density is related to the surface morphology.

Key words: Solar cell, dislocation, cathodoluminescence, metamorphic growth

INTRODUCTION

Heteroepitaxial growth is a powerful tool in exploring the potentials of various advanced electrical devices. For example, metamorphic growth allows us to connect various lattice-mismatched materials, and it has been applied to lasers, light-emitting diodes, transistors, and multi-junction solar cells.[1–4] High-efficiency multi-junction solar cells have also been realized using inverted metamorphic (IMM) growth, which enables combinations of materials (band-gap energies) that are more suited in terms of solar energy harvesting.[5,6] The IMM InGaP/GaAs/InGaAs triple-junction solar cell design has been considered for space applications and an actual flight demonstration has already been carried out in orbit.[7] In the metamorphic growth technique, graded buffer layers are introduced to release strain via dislocations and to confine the dislocations. It has been shown that dislocations extending to the wafer edge do not have an impact on the electrical characteristics of solar cells.[8] However, dislocations extending in the epitaxial growth direction constitute non-radiative recombination centers and reduce the device performance significantly.[9] For example, theoretical calculations have shown that the threading dislocation densities in thin film GaAs solar cells on silicon substrates should be below 10^6 cm^{-2} in order to obtain efficiencies larger than 18%.[10] Note that these types of

---

(Received February 28, 2020; accepted June 7, 2020;

lattice-mismatched solar cells have similar correlations between solar cell efficiency and threading dislocation density.[11] Because the threading dislocation density should not exceed a certain threshold, characterization of such defects is important for device development.

Cathodoluminescence (CL) and electron beam-induced current (EBIC) imaging have been used to observe threading and misfit dislocations in strained layers.[12–14] In the case of upright metamorphic lattice-mismatched solar cells, the device structure can be divided into three main regions (from top to bottom): solar cell layers, step-graded buffer layers, and substrate. To evaluate dislocations inside the buffer layers, the electron beam acceleration voltage must be high enough to penetrate the thick layer structure above the buffer layers. However, a higher acceleration voltage results in a lower spatial resolution.[15] To solve this problem, mechanical polishing of the sample edge at a shallow angle with respect to the substrate surface can be used.[16] After polishing at shallow angles, the buried layers are directly exposed and CL images that are almost equivalent to the commonly used cross-sectional view can be obtained. In this work, we investigate misfit and threading dislocations in the step-graded InGaP buffer layers of a metamorphic single-junction InGaAs solar cell by CL imaging of sample edges. We show that, owing to a mechanical polishing of the edges at different angles, it is possible to characterize the whole structure and also very thin layers. This can be achieved by characterization at sample positions with large and small polishing angles, respectively. In the present device, in the region near the InGaP overshoot layer, the density of the dark lines extending in the [1-10] direction is higher than that of the dark lines extending in the [110] direction. On the other hand, near the InGaAs base layer, the density of the dark lines extending in [110] is higher than that of the dark lines extending in [1-10]. We also briefly discuss the effect of the surface morphology of the dislocation stopping layer.

EXPERIMENTAL METHODS

For the present investigation, upright metamorphic single-junction InGaAs solar cells with a cell size of 1 cm × 1 cm were fabricated by metal organic vapor phase epitaxy (MOVPE). Figure 1 shows the sample structure of our solar cell. The device layers (from top to bottom) are: InGaP window layer, InGaAs emitter layer, InGaAs base layer, InGaP back surface field (BSF) layer, InGaAs/InGaP/InGaAs multi-layer structure, InGaP overshoot layer, InGaP step-graded buffer layers, and GaAs substrate. The doping densities in the overshoot layer and step-graded buffer layers are the same. The thickness of the overshoot layer is larger than that of a single layer in the step-graded buffer layer. The *p*-type GaAs (001) substrate used for growth had a micut of 2° towards the [100] direction. Fifty-two devices were fabricated from the wafer, and one sample with intermediate open-circuit voltage was chosen for the detailed investigation by CL microscopy. The device performance was characterized at 25°C using an AM0 solar simulator (WACOM WXS-130S-L2HV). Prior to the CL measurements, the sample was processed by a cross-section polisher (JEOL SM-09010), which used an Ar ion beam at low beam energies of 4 kV with a shield plate. This low-energy ion beam was chosen in order to reduce surface damages. We evaluated the ratio of layer thickness to the extension of the polished surface (which corresponds to the polishing angle) for each layer and found that the local polishing rates were almost the same for all layers. In the SE and CL measurements, the focus was adjusted to the center position of the SE images. It must be considered that, due to the polishing angle, the working distance changes from the top of the SE image to the bottom. In the case that the measurement is seriously influenced by this effect, the sample stage should be tilted to achieve a constant working distance. In the present work, the SE images were obtained without tilting the sample stage. The CL measurements were performed by the HORIBA MP32 CL system attached to a Hitachi SU6600 field-emission scanning electron microscope (FE-SEM). A silicon photomultiplier tube (PMT) was used for the detection of the short-wavelength emission of the InGaP buffer layers and an InGaAs PMT was used for

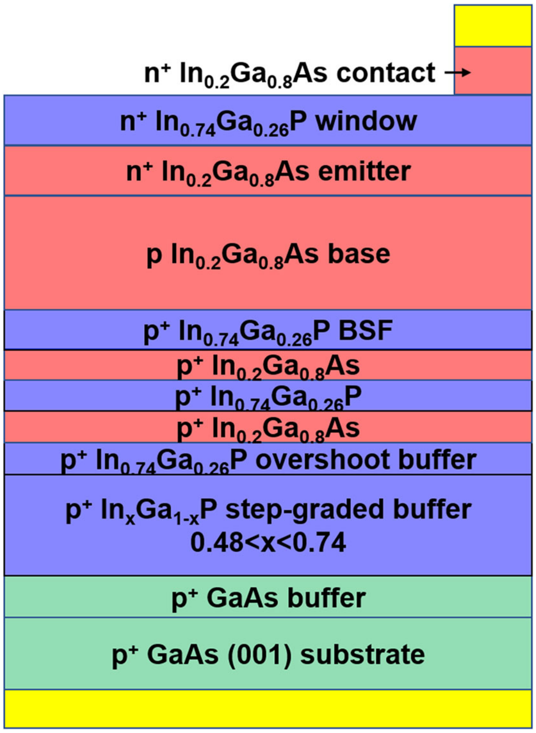

Fig. 1. Device structure of the upright metamorphic InGaAs solar cell. BSF: back surface field.

the detection of the long-wavelength emission of the InGaAs layers.

RESULTS AND DISCUSSION

Figure 2 plots the light current–voltage curve of the sample chosen for detailed evaluation. The open-circuit voltage (V_{oc}) provided by this device is 0.685 V. We additionally confirmed that there is a clear variation in the V_{oc} provided by the 52 cells from the single wafer; the maximum and minimum V_{oc} values are ≈ 0.715 V and 0.66 V, respectively. The V_{oc} distribution on the wafer has been attributed to the differences in the preferential glide planes of dislocations.[17] Figure 3a shows a schematic of the sample after polishing of the edge at an angle of 7.9°. The corresponding secondary electron image of the edge surface is provided in Fig. 3b. Figure 3c plots the CL spectrum depth dependence, which was recorded along the positions indicated with the yellow dots in Fig. 3b. Figure 3d–e present the schematic and data for the sample edge that was polished at 1.8°.

In Fig. 3b and e, the hetero-interfaces between the layers are relatively rough (for example, see the interface between the InGaAs base layer and the InGaP BSF layer). The curtaining effect[18] and also the surface morphology can cause this roughness. However, in this work, the direction of the Ar ion used to prepare the cross section was almost parallel to the x-axis of Fig. 3b and e. Therefore, the curtaining effect is considered to be negligible, and we attribute the interface roughness to the surface morphology. Further investigations of the hetero-interface are required to prove this assignment.

The data in Fig. 3b and c were obtained at room temperature using an acceleration voltage of 3 kV. In Fig. 3b, from bottom to top, we can clearly observe the GaAs substrate, the step-graded InGaP buffer layers, the InGaAs/InGaP/InGaAs multilayer structure (which acts as a dislocation stopping layer), the InGaP back surface field (BSF) layer, and the InGaAs base layer. The emission peak around 880 nm in Fig. 3c is from the GaAs layers shown at the bottom of the image in Fig. 3b. The emission peak that gradually changes from 680 to 760 nm from bottom to top, originates from the InGaP layers of the step-graded buffer. The strong peak around 760 nm is from the InGaP overshoot layer. Figure 3e and f show data obtained at 78 K using an acceleration voltage of 5 kV. Owing to the shallower polishing angle of th edge surface, we can clearly observe the InGaP overshoot layer, the dislocation stopping layer, the InGaP BSF layer, and the InGaAs base layer. The strong peak in Fig. 3f is assigned to the highly doped InGaAs layers in the dislocation stopping layer. In the following, we show results related to this region.

Figure 4a shows the secondary electron image obtained at 78 K using an acceleration voltage of 5 kV. This image covers the range from the InGaAs layer to the graded buffer layers (edge polishing angle ≈ 1.6°). Figure 4b shows the spectral intensity map, that provides the depth-resolved information along the positions of the yellow dots of the vertical arrow in Fig. 4a. The emission wavelength of the overshoot layer is observed at about 730 nm. The yellow cross marks indicate the emission peaks of four individual layers of the step-graded buffer. The wavelengths of these peaks are in the range of 730 to 680 nm in this sample region. The CL spectra of these four buffer layers and the overshoot buffer are shown in Fig. 4c. The relatively strong signal intensity of the overshoot layer is a result of its larger thickness. Note that all four buffer layers exhibit a relatively broad spectrum. For example, Fig. 4d shows that the spectrum taken at position #33 (Buffer 3) can be decomposed into two spectra with peaks at 703 and 691 nm. Since the other spectra can also be decomposed into two spectra here, we consider that the broad spectra occurs when two layers are simultaneously excited when the polishing angle with respect to the substrate surface is shallow and the penetration depth of the electron beam is larger than the layer thickness projected on the beam axis. Note that similar broad spectra were also confirmed for another sample when we used an acceleration voltage of 3 kV.

Figure 4e and f show the monochromatic CL images taken at 690 nm and 720 nm (spectral width ≈ 20 nm), respectively. These images show certain regions of the step-graded buffer, whose emission peak range is 680–760 nm. It is evident that the dark line density (DLD) in Fig. 4e is relatively large. In accordance with the abovementioned spectral analysis, it can be considered that the dark lines of at least two buffer layers are superimposed in this figure, because of the excitation of several buffer layers. Figure 4f shows the image of the overshoot layer and we can confirm that the DLD is relatively small in the region near the dislocation stopping layer (region near the top).

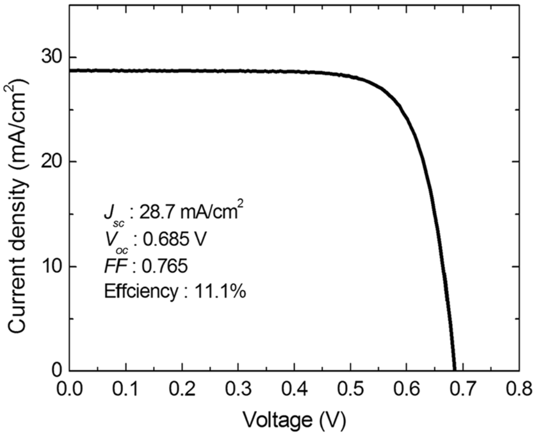

Fig. 2. Light current–voltage curve under 1 sun illumination (AM0) at 25°C. The short-circuit current (J_{sc}), open-circuit voltage (V_{oc}), fill factor (FF), and conversion efficiency are provided in the figure.

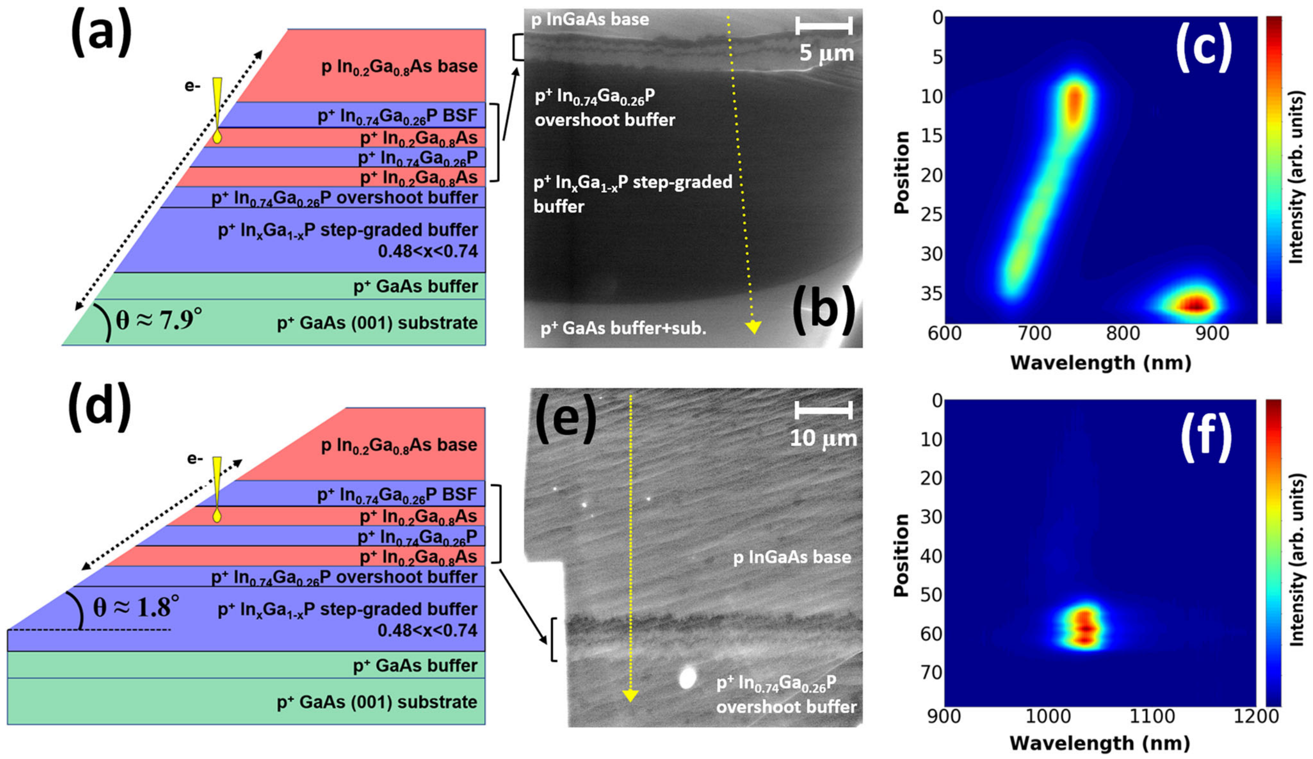

Fig. 3. (a), (d) Schematics of sample edges with large (≈ 7.9°) and small (≈ 1.8°) polishing angles, respectively. (b), (e) The corresponding secondary electron images of the edge surfaces. (c), (f) Depth dependence of the CL spectra. The data for these maps were obtained along the yellow dots shown in (b) and (e), respectively. The position in each map therefore represents the distance from the top of the CL images in (b) and (e) (Color figure online).

Here, the yellow arrows indicate positions of dark spots. The dark spots are discussed in more detail near the end of "Results and Discussion" section.

To visualize the highly doped InGaAs layers inside the dislocation stopping layer, we select the center wavelength 1035 nm according to the peak in Fig. 3f. The obtained monochromatic images of the sample edge, polished at an angle of less than 1.0°, are shown in Fig. 5. In this measurement, the sample temperature was 78 K and the images for the acceleration voltages of 5 kV, 7 kV, and 10 kV are shown in Fig. 5a, b, and c, respectively. In Fig. 5a, the dark spots and dark lines cannot be clearly observed, and there are many small bright blocks that are elongated along [110]. There is a possibility that these features reflect the surface morphology and the details are discussed at the end of this section. Since the acceleration voltage is not high enough to excite the two InGaAs layers inside the dislocation stopping layer, the emission intensity in Fig. 5a is low. As the acceleration voltage increases, the dark spots and dark lines become clearer. In order to analyze the highly doped InGaAs layers, we consider that an acceleration voltage of 10 kV is appropriate.

Figure 6a and b show monochromatic CL images taken at 1035 nm for an acceleration voltage of 10 kV. Since the imaging area of HORIBA MP32CL is limited, we combined two images in Fig. 6a. The dark regions at the bottom and top of the combined image correspond to the InGaP overshoot layer and the InGaAs base layer, respectively. They are dark, because the emission of the InGaP overshoot layer is below 800 nm (Fig. 3c) and the emission intensity of the InGaAs base layer is much weaker than the intensities of the InGaAs layers inside the dislocation stopping layer (Fig. 3f). Figure 6a shows that the behavior of dislocation generation depends on the sample depth. The horizontal red broken line represents the border between two regions with different features as explained in the following paragraphs. In the lower region, the density of dark lines that are aligned with the [1-10] direction is slightly higher than that of the lines aligned with the [110] direction ($\approx 4.8 \times 10^5$ cm^{-1} and $\approx 2.8 \times 10^5$ cm^{-1}, respectively). Furthermore, the average length of dark lines oriented along [1-10] is longer than that of the dark lines oriented along [110]. We attribute the difference in the average length to different dislocation generation velocities; the generation velocity of α dislocations, which extend in the [1-10] direction, is higher than that of β dislocations, which are aligned with the [110] direction.[19,20]

The reason for the more pronounced dark lines in the lower part of Fig. 6a is that here the emission from the InGaAs layer near the InGaP overshoot layer is obtained. On the other hand, in the upper

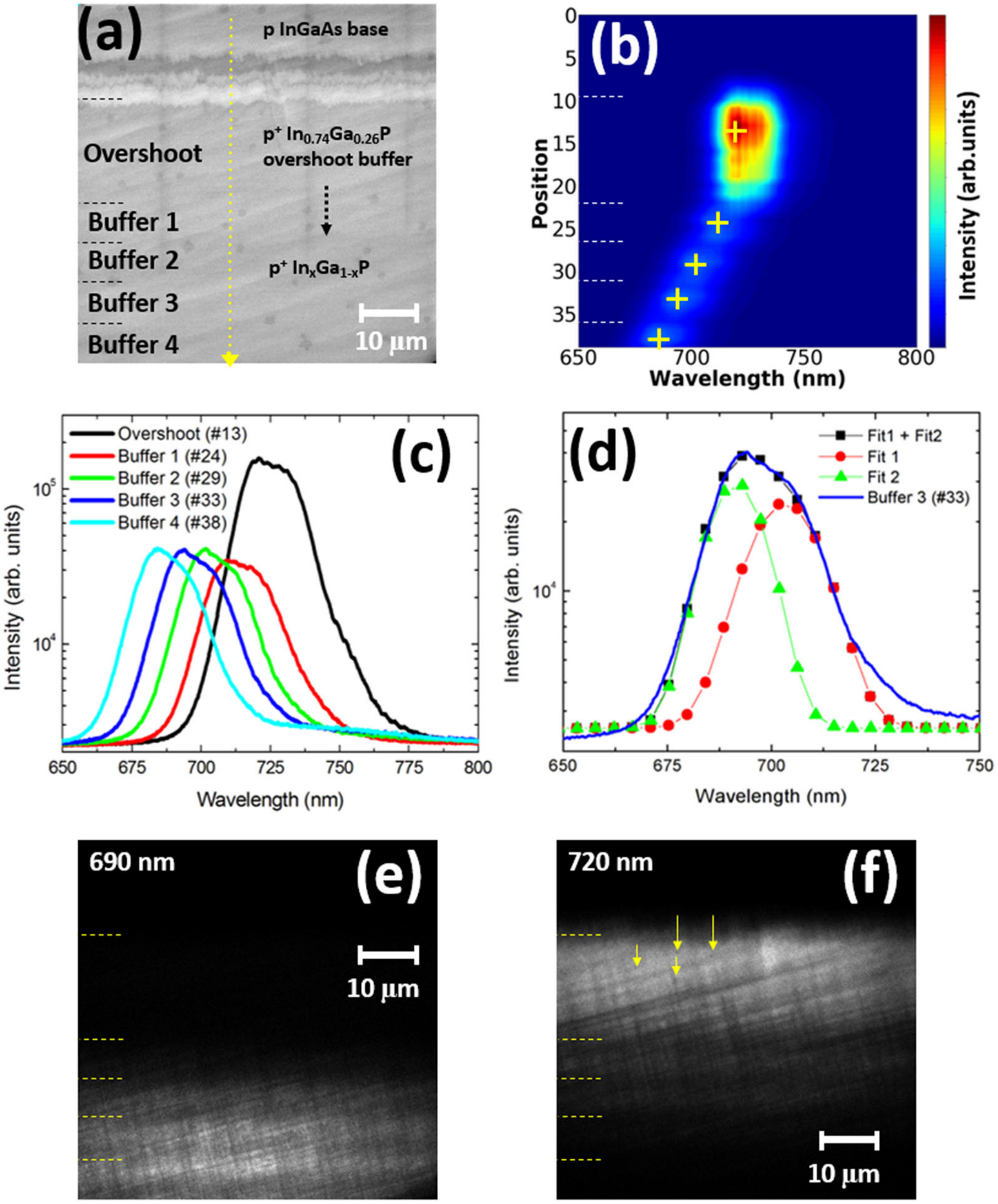

Fig. 4. (a) Secondary electron image of the edge surface obtained using a polishing angle of 1.6°. (b) Depth dependence of the CL spectrum. The spectra were recorded at the yellow dots shown in (a). (c) Spectra at the cross marks in (b). (d) Spectra recorded at positions #28, #29, #31, #32, and #33. Indicated in (b). (e), (f) Nearly monochromatic images at center wavelengths of 690 and 720 nm, respectively (Color figure online).

part, the electron beam cannot penetrate several layers until the lower InGaAs layer, and thus the dark lines in the upper part of the figure are relatively dim. We note that there are also dark spots in the upper and lower parts of Fig. 6a. The dark spots in the upper part are slightly larger than those in the lower part. One possible explanation for this is that the threading dislocations penetrate through several layers and some of them get very close to each other in the upper layer. To verify this model, it is necessary to record images with higher resolution in order to count the dark spots quantitatively. This approach may be useful to clarify how the threading and misfit dislocations move in the dislocation stopping layer.

In Fig. 6b we provide the magnified view of the marked rectangular area in Fig. 6a in order to investigate the upper region in more detail. In the magnified view, there are many small bright blocks that are elongated along [110]. This structure can be observed by using an lower acceleration voltage of 5 kV. It resembles the atomic force microscopy (AFM) image of the surface of the InGaAs metamorphic buffers reported in Ref. 21. It is known that the surface morphology is a result of the strain-energy minimization and the kinetics of surface

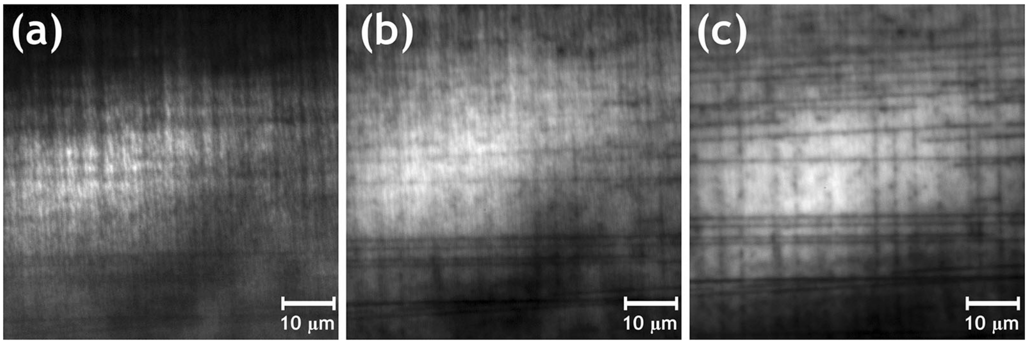

Fig. 5. Monochromatic CL images for three different acceleration voltages: (a) 5.0 kV, (b) 7.0 kV, and (c) 10.0 kV. The center wavelength is 1035 nm and the spectral width is about 20 nm.

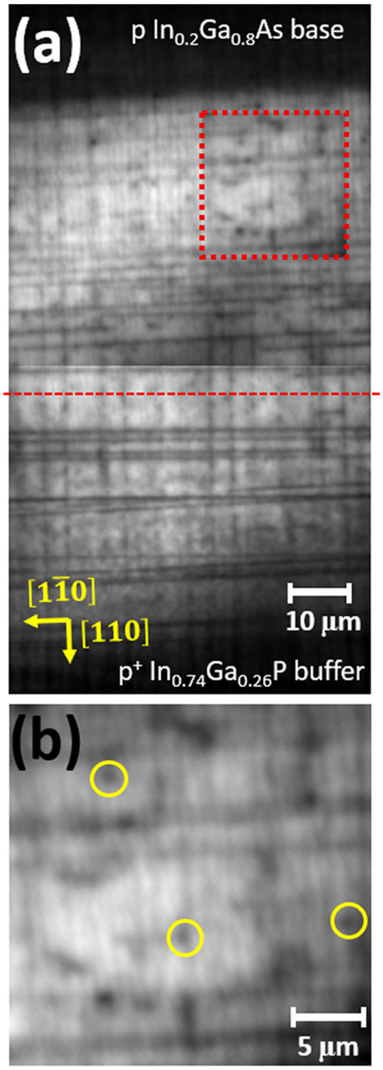

Fig. 6. (a) Monochromatic CL image for an edge with a polishing angle of less than 1.0°. The center wavelength is 1035 nm and spectral width is about 20 nm. The upper and lower regions are divided by the horizontal red broken line in order to indicate regions with different behavior. (b) The magnification of the area in the red rectangle shown in (a). The yellow circles show positions of several dark spots (Color figure online).

diffusion.[22] It is possible that the structure in Fig. 6b reflects the surface morphology caused by the strain. These surface features should be related to β dislocations, because the surface morphology extends in the [110] direction. Note that dark spots exist between the small bright blocks (see yellow circles in the figure). This is consistent with our interpretation, because surface morphology can lead to dislocation nucleation.[23,24] Therefore, it is necessary to carefully control the strain relaxation in order to suppress dislocation nucleation at the surface of the dislocation stopping layer.

CONCLUSIONS

In this study, we have investigated misfit and threading dislocations in a metamorphic upright single-junction InGaAs solar cell. by employing CL measurements on sample edges that had been polished at shallow angles, we were able to directly observe even very thin layers, in addition to the imaging of the entire sample at a position with a large polishing angle. By using this data, it was shown that the InGaAs/InGaP/InGaAs multi-layer structure in the present device can be divided into different regions according to their dislocation characteristics. In the region near the InGaP overshoot layer, the density of the dark lines extending in the [1-10] direction (α dislocations) was slightly higher than that of the lines extending in the [110] direction (β dislocations). In addition, the average length of the dark lines aligned with [1-10] was longer than that of the lines aligned with [110]. In the region near the InGaAs base layer, the density of the dark lines extending in the [110] direction was higher than that of the dark lines in the [1-10] direction. We discussed the relation between this result and the surface morphology of the InGaAs/InGaP/InGaAs multi-layer. The observed dark spots may be related to the stress concentration at the rough surface.

ACKNOWLEDGMENTS

The authors would like to express their sincere gratitude to Mr. M. Hata and Mr. T. Osada of Sumitomo Chemical Co., Ltd. and Mr. H. Washio of

SHARP Corporation for their support in preparing the solar cells. The authors would like to thank Mr. J. Harada and Mr. M. Sugai of AES Corporation for kind assistance with the solar cell characterization.

CONFLICT OF INTEREST

The authors declare that they have no conflict of interest.

REFERENCES

1. L.J. Mawst, J.D. Kirch, C.-C. Chang, T. Kim, T. Garrod, D. Botez, S. Ruder, T.F. Kuech, T. Erles, R. Tatavarti, N. Pan, and A. Wibowo, *J. Cryst. Growth* 370, 230–235 (2013).
2. T.M. Christian, D.A. Beaton, K. Mukherjee, K. Alberi, E.A. Fitzgerald, and A. Mascarenhas, *J. Appl. Phys.* 114, 074505 (2013).
3. M.L. Lee and E.A. Fitzgerald, *J. Appl. Phys.* 97, 011101 (2005).
4. R.M. France, F. Dimroth, T.J. Grassman, and R.R. King, *MRS Bull.* 41, 202–209 (2016).
5. J.F. Geisz, M.A. Steiner, K.L. Schulte, M. Young, R.M. France, and D.J. Friedman, *AIP Conf. Proc.* 2012, 040004 (2018).
6. R.M. France, J.F. Geisz, I. Garcia, M.A. Steiner, W.E. McMahon, D.J. Friedman, T.E. Moriarty, C. Osterwald, J.S. Ward, A. Duda, M. Young, and W.J. Olavarria, *IEEE J. Photovolt.* 6, 578 (2016).
7. T. Sumita, Y. Shibata, T. Nakamura, K. Shimazaki, A. Kukita, M. Imaizumi, S. Sato, T. Ohshima, and T. Takamoto, Jpn. J. Appl. Phys. 57, 08RD01 (2018).
8. R.M. France, J.F. Geisz, M.A. Steiner, B. To, M.J. Romero, W.J. Olavarria, and R.R. King, *J. Appl. Phys.* 111, 103528 (2012).
9. R. Oshima, Y. Watanabe, M. Yamanaka, H. Kawanami, I. Sakamoto, K. Matsubara, and I. Sakata, *J. Cryst. Growth* 378, 226 (2013).
10. M. Yamaguchi and C. Amano, *J. Appl. Phys.* 58, 3601 (1985).
11. C.L. Andre, D.M. Wilt, A.J. Pitera, M.L. Lee, E.A. Fitzgerald, and S.A. Ringel, *J. Appl. Phys.* 98, 014502 (2005).
12. K.L. Schulte, H.L. Guthrey, R.M. France, and J.F. Geisz, *IEEE J. Photovolt.* 10, 109 (2020).
13. X.L. Yuan, T. Sekiguchi, J. Niitsuma, Y. Sakuma, S. Ito, and S.G. Ri, *Appl. Phys. Lett.* 86, 162102 (2005).
14. K.N. Yaung, M. Vaisman, J. Lang, and M.L. Lee, *Appl. Phys. Lett.* 109, 032107 (2016).
15. K. Kanaya and S. Okayama, *J. Phys. D Appl. Phys.* 5, 43 (1972).
16. J. Chen, W. Yi, T. Kimura, S. Takashima, M. Edo, and T. Sekiguchi, *Appl. Physic. Express* 12, 051010 (2019).
17. A. Ogura, H. Suzuki, and M. Imaizumi, *J. Cryst. Growth* 533, 125432 (2020).
18. T. H. Loeber, B. Laegel, S. Wolff, S. Schuff, F. Balle, T. Beck, D. Eifler, J. H. Fitschen, and G. Steidl, J. Vac. Sci. Technol. B, 35, 06GK01 (2017).
19. K.R. Breen, P.N. Uppal, and S. Ahearn, *J. Vac. Sci. Technol. B* 7, 758 (1989).
20. H. Suzuki, T. Sasaki, A. Sai, Y. Ohshima, I. Kamiya, M. Yamaguchi, M. Takahashi, and S. Fujikawa, *Appl. Phys. Lett.* 97, 041906 (2010).
21. R. Kumar, A. Bag, P. Mukhopadhyay, S. Das, and D. Biswas, *Appl. Surf. Sci.* 357, 922 (2015).
22. E.A. Fitzgerald, S.B. Samavedam, Y.H. Xie, and L.M. Giovane, *J. Vac. Sci. Technol., A* 15, 1048 (1997).
23. A.G. Cullis, A.J. Pidduck, and M.T. Emeny, *J. Cryst. Growth* 158, 15–27 (1996).
24. D.E. Jesson, S.J. Pennycook, J.-M. Baribeau, and D.C. Houghton, *Phys. Rev. Lett.* 71, 1744 (1993).